Optics and Lasers in Engineering 154 (2022) 107016

Contents lists available at ScienceDirect

Optics and Lasers in Engineering

journal homepage: www.elsevier.com/locate/optlaseng

Femtosecond laser micromachining of suspended silica-core liquid-cladding waveguides inside a microfluidic channel

João M. Maia[a,b,*], Duarte Viveiros[a,b], Vítor A. Amorim[c], P.V.S. Marques[a,b]

[a] CAP - Centre for Applied Photonics, INESC TEC, Porto 4150-179, Portugal
[b] Department of Physics and Astronomy, University of Porto, Porto 4169-007, Portugal
[c] Sphere Ultrafast Photonics, Porto 4169-007, Portugal

ARTICLE INFO

Keywords:
Femtosecond laser micromachining
Fused silica
Mach-Zehnder interferometer
Suspended waveguide
Wet etching

ABSTRACT

This work addresses the fabrication of straight silica-core liquid-cladding suspended waveguides inside a microfluidic channel through fs-laser micromachining. These structures enable the reconfiguration of the waveguide's mode profile and enhance the evanescent interaction between light and analyte. Further, their geometry resembles a tapered optical fiber with the added advantage of being monolithically integrated within a microfluidic platform. The fabrication process includes an additional post-processing thermal treatment responsible for smoothening the waveguide surface and reshaping it into a circular cross-section. Suspended waveguides with a minimum core diameter of 3.8 μm were fabricated. Their insertion losses can be tuned and are mainly affected by mode mismatch between the coupling and suspended waveguides. The transmission spectrum was studied and it was numerically confirmed that it consists of interference between the guided LP_{01} mode and uncoupled light and of modal interference between the LP_{01} and LP_{02} modes.

1. Introduction

Optofluidic devices are a class of systems which combine integrated optics with microfluidics. These devices can be used for photonics or biosensing applications, and often rely on the interaction between the traveling optical beam and the analyte circulating inside the microfluidic channel [1]. Two distinct configurations are usually designed to achieve this interaction. In one case, light is launched into the microfluidic channel by optical waveguides designed external to it. Examples of these devices include Mach-Zehnder interferometers [2], Fabry-Pérot cavities [3] and optical tweezers [4]. The other configuration consists in fabricating the waveguide, formed by a solid-core and liquid-cladding, inside the microfluidic channel [5,6].

The latter option provides a way for the fluid to directly interact with the optical mode(s) travelling across the waveguide. Compared to solid-core solid-cladding waveguides, this property can be used to design reconfigurable waveguides where their mode profile can be tuned by changing the refractive index of the cladding. Also, in contrast to liquid-core solid-cladding waveguides and to all-liquid waveguides, it is easier to find liquids with a refractive index smaller than that of the core [7,8] and there is no need for constant laminar flow to avoid mixing between the core and cladding, respectively. Suspended waveguides can also be exploited for sensing applications, where variations in the properties of the analyte (refractive index, absorbance or concentration of species) can be monitored through measurement of the transmission spectrum [6,9,10] or of the emitted fluorescence [11]. This geometry can also be used to design cantilevers or monolithic oscillators for application in vibration monitoring [12] and optical modulation [13], or to form optical phase-shifters where thermal isolation enhances the performance of the device [14]. Lastly, suspended waveguides can also be used to excite optical modes of nearby resonators also integrated inside a microfluidic channel [5,15].

Due to the possibility of forming three-dimensional structures with high resolution and in a user-defined geometry, fs-laser micromachining has been preferentially used to fabricate these devices. In particular, polymeric and glass waveguides have already been demonstrated via water-assisted laser ablation [14], two-photon polymerization triggered by fs-laser irradiation [15] and fs-laser irradiation followed by chemical etching [16]. Despite the recent progress made to multiphoton polymerization, glasses are still better suited to this function as a result of their optical, mechanical and thermal properties and due to their biocompatibility and inertness to most solvents. Still, glass machining has its own issues. The machined surface usually has a roughness of around 100 nm and is characterized by a long-range modulation related to the laser di-

* Corresponding author at: CAP - Centre for Applied Photonics, INESC TEC: Instituto de Engenharia de Sistemas e Computadores Tecnologia e Ciencia, Departamento de Física, Rua do Campo Alegre 687, 4150-179 Porto, Portugal

E-mail addresses: joao.m.maia@inesctec.pt (J.M. Maia), carlos.d.viveiros@inesctec.pt (D. Viveiros), vamorim@sphere-photonics.com (V.A. Amorim), psmarque@fc.up.pt (P.V.S. Marques).

https://doi.org/10.1016/j.optlaseng.2022.107016
Received 2 December 2021; Received in revised form 27 January 2022; Accepted 27 February 2022
Available online 7 March 2022
0143-8166/

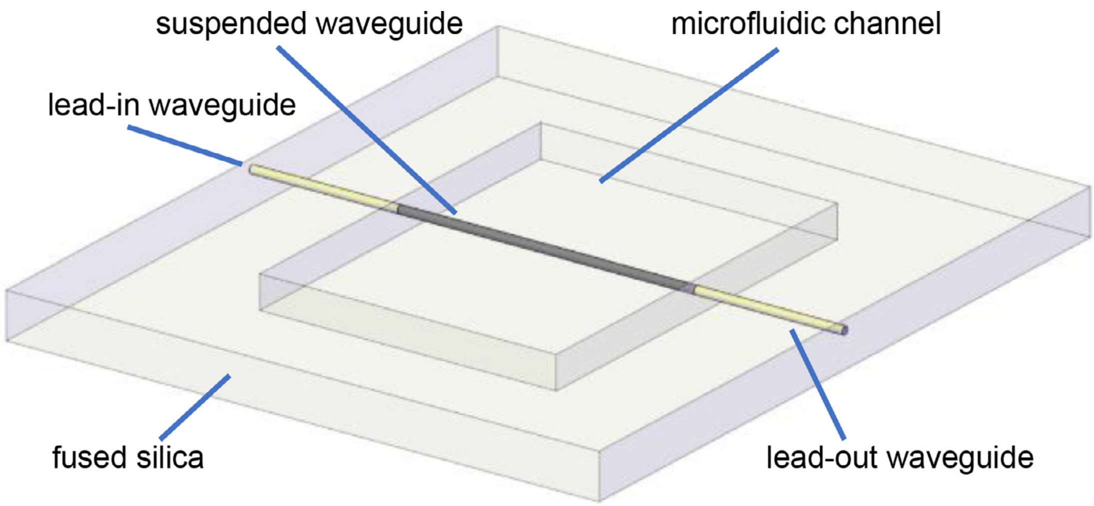

Fig. 1. Schematic of the device.

rect writing pattern [8]. This, in turn, translates into optical scattering that increases the propagation losses. Further, since it relies on subtractive processes, namely etching or ablation, the fabrication of micrometric structures is seldom discussed. In fact, most papers only consider the fabrication of suspended waveguides with a core diameter between 20 and 50 μm [12,16]. This prevents a higher interaction between the optical mode and the analyte, which can be obtained if the penetration depth of the evanescent field is larger, for instance, by decreasing the diameter of the core.

Here, this issue is addressed and the fabrication of silica-core liquid-cladding waveguides with a core diameter between 4 and 10 μm is described. Their guiding characteristics are studied against the refractive index of the cladding medium. The potential use of this device as a Mach-Zehnder interferometer for optical sensing is also considered.

2. Experimental Procedure

A schematic of the device is shown in Fig. 1. It consists of a silica core suspended inside a microfluidic channel and anchored to its lateral walls. The core is entirely surrounded by a fluid, whose refractive index is lower than that of fused silica, and which serves as cladding. This way, light can be guided along the suspended core. Two fs-laser written waveguides, named lead-in and lead-out, assure coupling of light into and out of the suspended waveguide, respectively.

The "negative" image of the final device is first imprinted on a fused silica substrate (Suprasil 1), with dimensions of 25 × 25 × 1 mm^3 and with its facets polished, via laser direct writing taking place in a Workshop of Photonics workstation. A 0.42 numerical aperture plan achromat objective (Mitutoyo M Plan Apo NIR 50 ×) focuses the 515 nm laser beam (Satsuma HP, Amplitude Systèmes), composed by a train of 250 fs long pulses at a repetition rate of 500 kHz, inside the substrate. The substrate is mounted on Aerotech direct-drive stages (ANT130XY-110 PLUS and ANT130V-5 PLUS), which translate the sample relative to the beam focus. The three-dimensional design of the microfluidic channel is sliced into several horizontal layers periodically spaced by 5 μm, and then further hatched into parallel tracks uniformly distanced by 3 μm. Each track is written with a pulse energy of 60 nJ, scanning speed of 3000 μm/s, and with the incident beam polarized orthogonally to the scanning direction in order to speed up the etching reaction and minimize the surface roughness of the machined surface. The layers are written sequentially from bottom to top, while tracks within each layer are scanned following the same direction. In the layers beneath and above the suspended waveguide, the tracks are oriented perpendicular to the waveguide's axis to facilitate the removal of debris during etching and to minimize the writing time, respectively. Regarding the layers containing the suspended waveguide, these are scanned parallel to the axis of the waveguide to minimize sidewall roughness. Following this design, the written suspended cores have a square shape. Further, given that the cross-section of a single laser-modified track has an elliptical shape with dimensions of 2 μm by 11 μm, the width and height of the suspended core are offsetted by these values from the initial design.

Chemical etching is then performed by immersing the substrate for 40 minutes in an ultrasonic bath (Branson 2510 ultrasonic cleaner) of hydrofluoric acid in a 10% volumetric concentration and at a temperature of 30±5°C. During this reaction, the laser-modified volume is etched at a faster rate than the pristine medium, which leaves behind a suspended core, as shown in Fig. 2(a). Albeit the suspended core preserves its initial shape, the etchant also attacks the pristine medium at a rate of 0.1 μm/min which leads to a slight decrease in the cross-sectional dimensions of the core. Fig. 2.(a) also shows a periodic relief pattern on the etched surface of the suspended core with a period of 3 μm along the axis of the waveguide, which coincides with the spacing between adjacent laser-written tracks and with their scanning direction. Further surface profile measurements, made with a Dektak Bruker profilometer, revealed an RMS roughness of 87 nm. The roughness of the sidewall is lower due to the layer-to-layer spacing being smaller than the height of a single laser-modified track, which improves the spatial resolution along the vertical direction. Nevertheless, the waviness on the top and bottom surfaces is directly related to optical scattering, which is linked to an increase in the propagation losses of the waveguide.

To reduce the roughness, thermal annealing is conducted after chemical etching. This procedure is performed in a closed furnace (Carbolite RHF-1500) at atmospheric pressure, where the temperature of the substrate is gradually raised to a dwell temperature of 1250°C at an initial heating rate of 15°C/min that falls to less than 1°C/min as the temperature of the furnace gets closer to the setpoint value. The substrate is then kept at 1250°C for an additional five hours, before cooling down slowly back to room temperature. During this process, surface tension overcomes thermally decreasing viscosity forces leading to material redistribution as to minimize its surface free energy [17]. This has three effects on the morphology and shape of the suspended waveguide. As shown in Fig. 2(b), the machined surface becomes uniform and smooth, with surface profile measurements revealing that the RMS roughness decreases from 87 to 11 nm with this treatment [5]. Second, material reflow driven by surface tension and a decreasing material's viscosity, gradually morph the suspended waveguides into a new shape that minimizes their surface area [18]. This process, however, should not change the cross-sectional area of the suspended waveguide, which is

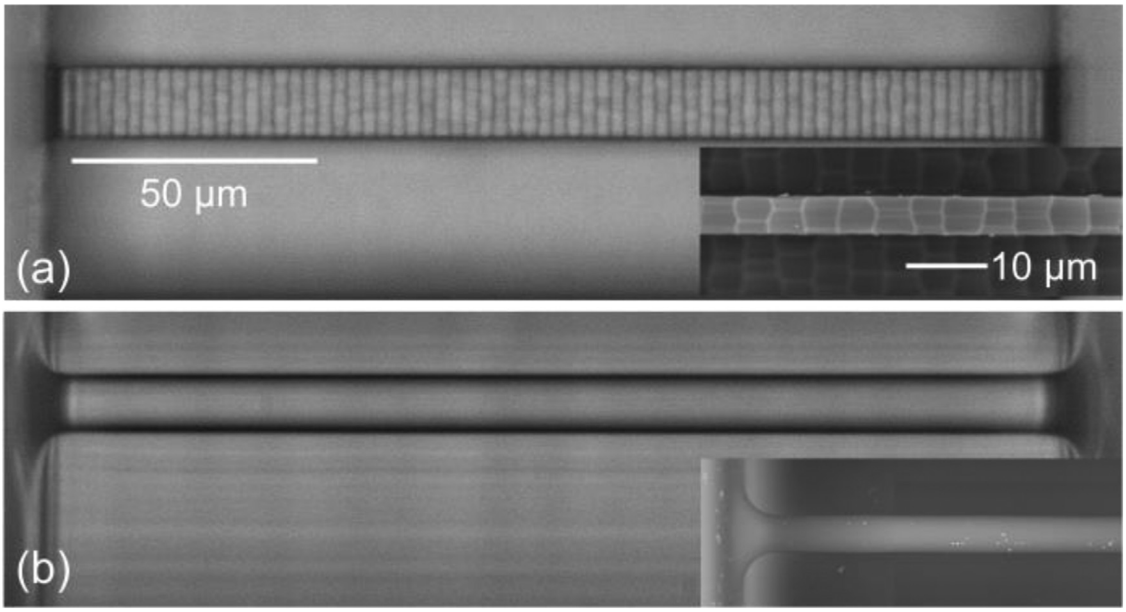

Fig. 2. Top view image of a 205 μm long suspended waveguide with a core diameter of 13.6 μm (a) after chemical etching and (b) after thermal annealing. The insets correspond to top view Scanning Electron Microscopy images of a 100 μm long suspended waveguide with a core diameter of 7.9 μm; these were obtained with a Hitachi FlexSEM1000 microscope operating at low vacuum and in backscattered electron mode.

the same before and after thermal treatment. Knowing the designed geometry and dimensions of the suspended core and having measured its width/diameter before and after this process, it was established that the cross-section had to evolve from a square into a circular-shape during this procedure. Lastly, for lengths smaller than ≈2 mm, the cores remain stable and straight after thermal annealing. However, suspended waveguides longer than 2 mm bent downwards during thermal treatment. For instance, suspended waveguides with length between 2 mm and 5 mm ended up with a curvature radius of around 450 mm, which should not add significant optical losses. A similar issue has already been reported by Cheng *et al* [16], who solved it by fabricating 100 μm long periodically spaced pedestals, whilst still experiencing an additional optical loss of 0.12 dB/pedestal at 633 nm.

Lastly, 1.1-1.2 cm long lead-in and lead-out waveguides are written following the same laser direct writing protocol, with a pulse energy of 100 nJ, scanning speed of 200 μm/s and with the incident beam polarized parallel to the scanning direction. These inscription conditions are known to produce low-loss waveguides at 1550 nm, with coupling losses to a SMF28 fiber and propagations losses of 0.36 dB/facet and 0.33 dB/cm, respectively [19]. To avoid the “Quill” effect [20], both waveguides are written along the same direction, with the lead-in/lead-out waveguide written headed into/away from the microfluidic channel, respectively. Some additional considerations are made to minimize coupling losses between the lead-in/lead-out waveguide and the suspended waveguide due to geometrical misalignment. The optical axes of all waveguides are parallel to each other with an angular deviation error of less than 0.5°, and are aligned along the horizontal and vertical directions within a 0.1 μm and 1 μm error, respectively. Further, the lead-in and lead-out waveguides terminate 20 μm from the border of the microfluidic channel to avoid focusing mismatch and energy depletion near these interfaces. Finally, this procedure occurs after thermal annealing to prevent the waveguides from being erased during the latter [21].

To measure the insertion losses of the waveguide, light from an unpolarized broadband source (ASE source EXFO IQ-203 with module IQ-2300) is coupled to a single-mode fiber whose loose end is butt-coupled to the entrance of the lead-in waveguide. Meanwhile, light guided through the lead-out waveguide is coupled into another SMF-28 fiber and collected by an optical spectrum analyzer (ANDO AQ-6135B). The input/output fibers and the substrate rest on Elliot Martock MDE 881 stages with piezo controls (Dali E-2100), which enable precise alignment between the optical fibers and the respective waveguides. Index matching liquid (Cargille series AA $n_D^{25^\circ C} = 1.4580 \pm 0.0002$) was used to minimize Fresnel reflection at the interface between the input/output fiber and the lead-in/lead-out waveguide, respectively. The measured spectra, acquired from 1500 nm to 1600 nm with a resolution of 0.1 nm, are normalized to the profile losses of the optical source. To characterize the device against the refractive index of the surrounding fluid, the transmission spectrum is measured while successively adding different Cargille refractive index oils, with refractive index spanning from $n_D^{25^\circ C}$=1.3000 to $n_D^{25^\circ C}$=1.4520, to the microfluidic channel. In between measurements, the device is cleaned to avoid surface contamination. Before adding a new fluid, the transmission spectrum of an empty microfluidic channel is also measured and compared to a reference one to assure no surface fouling.

3. Experimental Results and Discussion

Several suspended waveguides with a length of 492 μm and with a circular cross-section with diameter spanning from 3.8 to 13.0 μm were fabricated inside a microfluidic channel at a depth of 75 μm (measured from the surface of the substrate to the center of the suspended waveguide). The insertion losses of the waveguides against the refractive index of the surrounding fluids are depicted in Fig. 3, together with the insertion losses of a straight fs-laser written waveguide that serves as reference.

As anticipated, the insertion losses are always higher than the losses of the reference fs-laser written waveguide. Unexpectedly, though, the gathered spectra reveal a periodical modulation. The period increases as the refractive index contrast lowers and is independent from the diameter of the suspended core. Further, the amplitude of the modulation seems to decrease as the diameter of the suspended core broadens, regardless of the cladding medium. Moreover, in Fig. 3(f-g), the insertions losses seem to be approximately constant over the entire measurement window for all diameters of the suspended core.

To understand Fig. 3, we first state that the insertion loss depends on multiple factors: (1) coupling losses between the input/output fiber and the lead-in/lead-out waveguide, respectively, (2) propagation losses

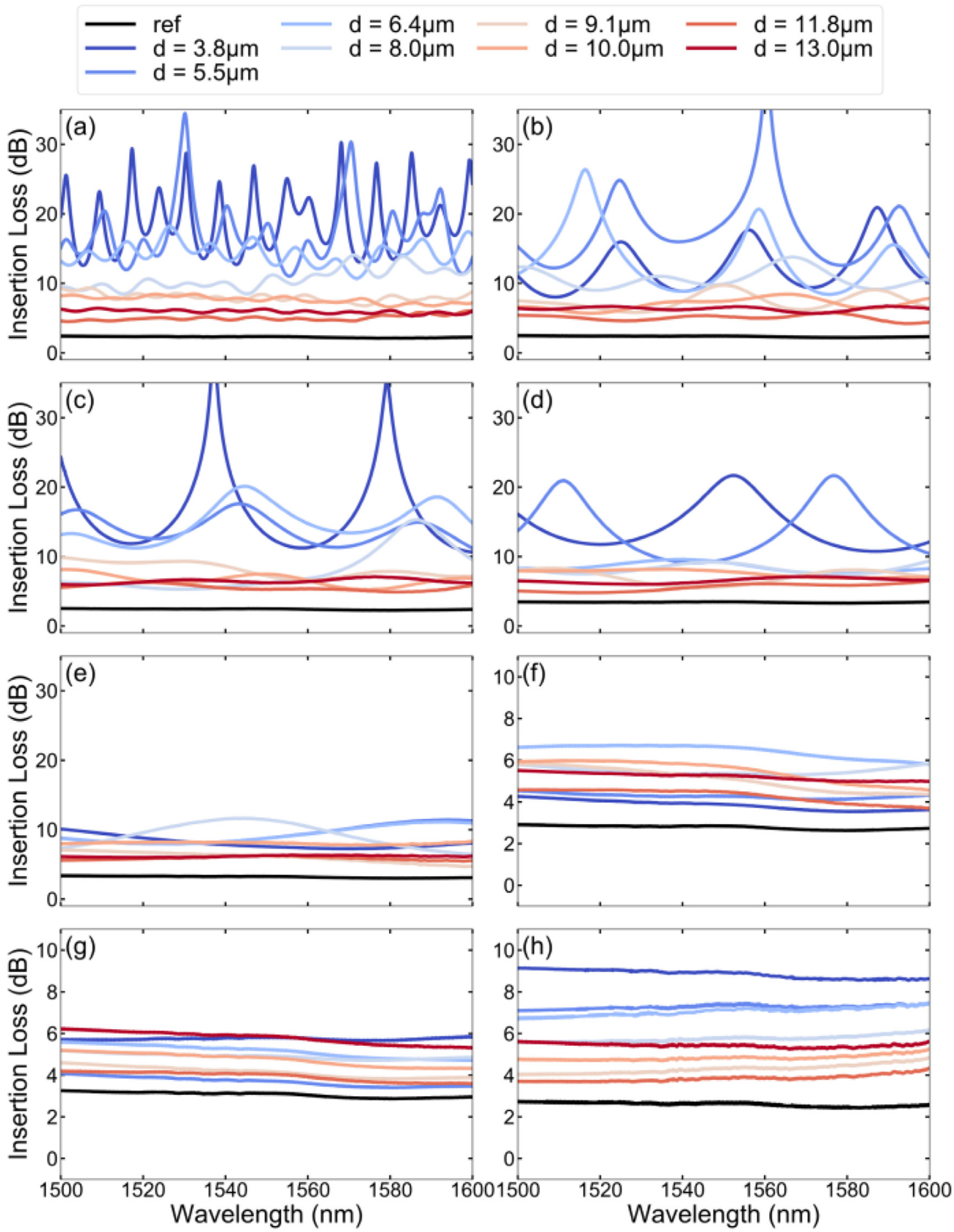

Fig. 3. Insertion losses of 492 μm long suspended waveguides with a core diameter spanning from 3.8 to 13.0 μm (a) with the microfluidic channel empty, and surrounded by a fluid with refractive index at 1550 nm of (b) 1.3150, (c) 1.3540, (d) 1.3900, (e) 1.4220, (f) 1.4340, (g) 1.4380 and (h) 1.4420. To facilitate the analysis, plots (a-e) have a different y-scale from the plots (f-h).

across the lead-in and lead-out waveguides, (3) coupling losses between the lead-in/lead-out waveguide and the suspended waveguide, (4) propagation losses of the suspended waveguide, and (5) evanescent absorption of the cladding medium. Factors (1) and (2) are common to all suspended waveguides regardless of their diameter. Still, it is noted that there are some variations in-between the insertion losses of the lead-in/lead-out waveguides due to the conditions in which they are written. These waveguides are written after chemical etching and thermal annealing at which point the surface of the fused silica substrate ceases to be uniform, resulting in the focusing depth of the fs-laser beam slightly varying during writing and in higher propagation losses. Also, when focusing the fs-laser beam at the edges of the substrate, there is a refractive index discontinuity that leads to the waveguide being written with an effective lower pulse energy near the facets and in a slightly higher coupling loss. Although this issue could be solved by polishing the facets of the substrate after laser direct writing of the lead-in/lead-out waveguides, doing so could risk damaging the suspended waveguides. Still, both of these issues only lead to a uniform and random increase of the insertion losses related to the lead-in/lead-out waveguides and do not explain the modulation observed in Fig. 3. Factor (4) can be neglected due to the realization of thermal annealing which decreases the surface roughness and minimizes optical scattering. Also, the chosen fluids have negligible absorption within the measurement window, which excludes factor (5).

Regarding factor (3), the coupling loss between the lead-in/lead-out waveguides and the suspended waveguide depends on any mode mismatch and on geometrical misalignment between them. Given that the coupling waveguides are written centered to and axially aligned with the suspended waveguide, it is expected that the insertion losses are mainly a result of mode mismatch between the lead-in/lead-out and the suspended waveguide [22]. This is further validated by noting that when changing the diameter of the core or the refractive index of the cladding, the mode profile of the suspended waveguide also changes which directly leads to a different insertion loss. Moreover, mode mismatch may also explain the modulation observed at the output. Mach-Zehnder interference between light that is coupled and guided across the suspended waveguide and light that is uncoupled and propagates across the microfluidic channel can cause the sinusoidal-shaped signal. Given that the microfluidic channel is narrow and the suspended waveguide is straight, uncoupled light travels almost parallel to the suspended waveguide, and both beams can therefore recombine at the lead-out waveguide. Uncoupled light travels along a medium with a refractive index defined by the fluidic solution, whereas one or more optical modes are guided along the suspended waveguide, each with a specific effective refractive index. Further, both arms of the interferometer have the same physical length. This situation is similar to what has been reported in in-line all-fiber Mach-Zehnder interferometers, constructed by splicing two single-mode fibers with a specific lateral offset and relying on the interference between the fundamental core mode and the excited cladding modes [23,24].

To show the importance of factor (3) on the data shown in Fig. 3, the theoretical coupling loss (CL) between the lead-in/lead-out and the suspended waveguide is first computed from Eq. (1):

$$CL = -10\log_{10}\left(\frac{4\mathrm{MFD}^2 d_x d_y}{\left(\mathrm{MFD}^2 + {d_x}^2\right)\left(\mathrm{MFD}^2 + {d_y}^2\right)}\right) \tag{1}$$

where MFD is the mode field diameter of the circular suspended waveguide, and d_x and d_y are the mode field diameters of the lead-in/lead-out waveguides along the horizontal and vertical direction, respectively [22]. Eq. (1) assumes no geometrical mismatch and that only the fundamental modes can propagate through both waveguides. The mode field of the lead-in/lead-out waveguides are equal as these are written with the same parameters. To measure the values d_x and d_y, a microscope objective is placed at the end of the lead-out waveguide which focuses the light beam into a CCD camera. The mode field is retrieved by fitting the measured intensity profile with a Gaussian function and by determining its width at $1/e^2$ of its maximum. The diameters d_x and d_y correspond to 7.0 μm and 12.5 μm, respectively; the directional dependence is due to the lead-in/lead-out waveguides possessing an elliptical cross-section [19]. The device geometry prevents performing the same measurement for the suspended waveguide. Instead, its mode field diameter was estimated through simulations made with COMSOL Multiphysics, which only requires knowledge over the geometry and refractive indices of the waveguide. In these calculations, it was considered a suspended waveguide with circular cross-section and core diameter equal to the experimentally measured values. The refractive indices of the core and cladding are equal to the refractive indices of fused silica (1.4440) and of the tested Cargille fluids at 1550 nm, respectively. Fig. 4 shows the simulated coupling loss curves.

From Fig. 3(a-d), when the refractive index of the cladding is smaller than 1.4, both the insertion losses and the amplitude of the modulated signal decrease as the diameter of the suspended core increases. These observations agree with the theoretical data which read that the coupling losses should increase as the diameter of the core reduces. Further, due to the high index contrast, the mode field is mostly confined to the core which explains why the insertion and coupling losses in Figs. 3 and 4, respectively, barely change with the cladding's refractive index for a given diameter. Assuming that the modulation pattern is due to Mach-Zehnder interference between guided and non-guided light, the behaviour of the fringe visibility is also expected. As the diameter of the suspended core increases, more light is coupled into the suspended waveguide and less into the remaining arm of the interferometer. Consequently, in spite of both arms having the same physical length, an imbalance between the power guided across both arms starts to occur, which translates in a decrease in the amplitude of the modulation. This issue is further aggravated by noting that, as the diameter of the core increases, the cross-sections of the lead in/lead-out and of the suspended waveguide start overlapping with one another, which causes an even lower fraction of the optical power that travels unguided across the channel to be recoupled into the lead-out waveguide.

The behaviour becomes different as the refractive index of the cladding gets closer to the refractive index of fused silica. In Fig. 3(f), the insertion losses increase as the core widens from a diameter of 3.8 μm to 6.4 μm before decreasing again as the diameter keeps rising, whereas in Fig. 3(g) the insertion losses decrease from a diameter of 3.8 μm to around 9-10 μm before rising again. Meanwhile in Fig. 3(h), the insertion losses seem to decrease as the diameter of the suspended core increases. These general trends are quite similar to the behaviour displayed in Fig. 4, which indicates that coupling loss between the lead-in/lead-out and the suspended waveguide is the main factor behind the measured loss profile in Figs. 3(f-h). Further, a minimum excess loss of 0.88, 0.73 and 0.86 dB was measured for a diameter of 11.8, 5.5 and 3.8 μm and surrounding refractive index of 1.4420, 1.4380 and 1.4340 at 1550 nm, respectively. The diameter at which these minima occur also seems to agree well with the expected theoretical diameter for minimum coupling loss. A more in-depth quantitative analysis cannot be done due to uncertainty in separating the insertion losses only related to the suspended waveguide to those only linked to the lead-in/lead-out waveguides.

Still, to confirm the origin of the modulation in the spectra of Fig. 3, another device was fabricated consisting of 504, 1012 and 2014 μm long suspended waveguides, each made in their respective microfluidic channels at a depth of 70 μm, with a circular cross-section and with an average diameter of 6.7±0.3 μm. The insertion losses of the three waveguides are plotted in Fig. 5 for different cladding media. Again, a main oscillation is observed, whose period increases non-linearly as the external refractive index rises towards the core's refractive index. Further, the free spectral range decreases by a half and a fourth as the length of the suspended waveguide doubles and quadruples, respectively. Both results are expected for a balanced Mach-Zehnder interferometer. These observations are also summarized in Fig. 6, where the scatter points represent the period of the modulation directly measured from the gathered spectra. Given that in some of the spectra, such as in Fig. 5 (a), a secondary modulation is observed, a high-pass filter is first applied in these cases to facilitate the measurement of the free spectral range. Further, in the plots where only one maximum and/or one minimum is retrieved, the period is estimated as double the difference between the former wavelengths. Both of these features explain why some points have a larger margin of error. Also, no period is retrieved for the spectra of the 504 and 1012 μm long suspended waveguides when surrounded by liquids with refractive index of 1.4420, as the insertion losses seem constant in the 1500 to 1600 nm window, with the free spectral range, therefore, being much larger than this range.

The measured period is then compared with the expected free spectral range, considering Mach-Zehnder interference between the fundamental mode of the suspended waveguide and light that travels unguided across the microfluidic channel. Theoretically, and assuming that the optical power in both arms of the interferometer is identical, the in-

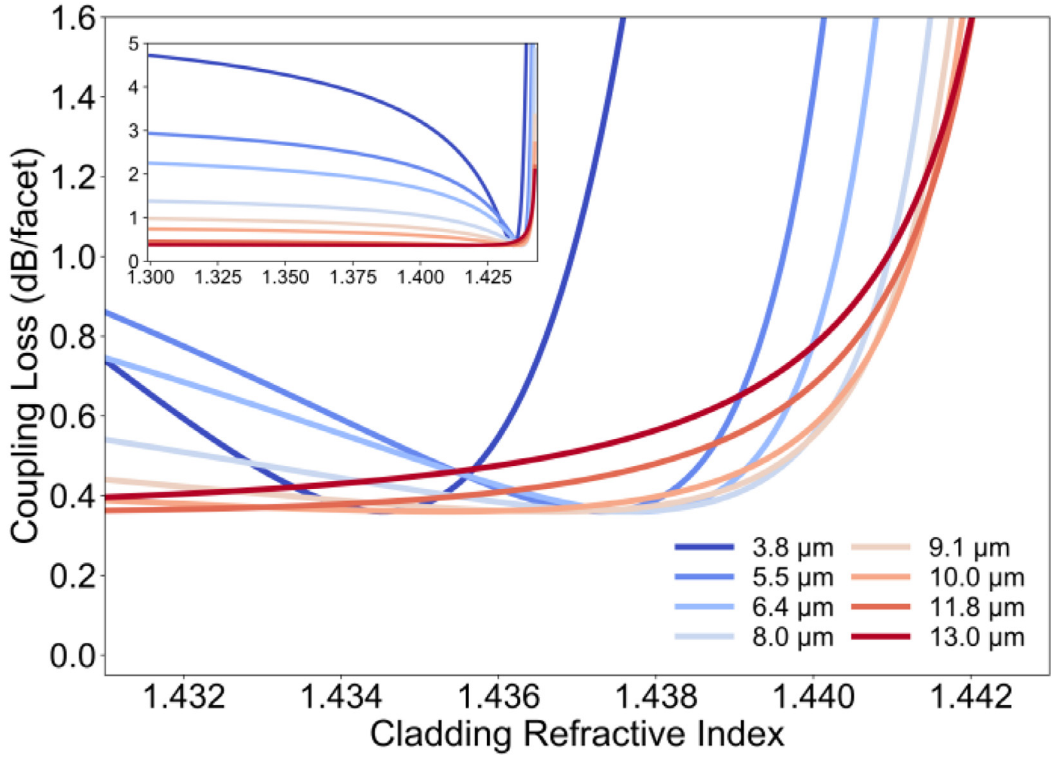

Fig. 4. Theoretical coupling losses at 1550 nm between the lead-in/lead-out and the suspended waveguide, obtained after solving Eq. (1). The data is plotted against the refractive index of the fluid surrounding the suspended core and for different core diameters. The inset image is a zoom-out of the main plot.

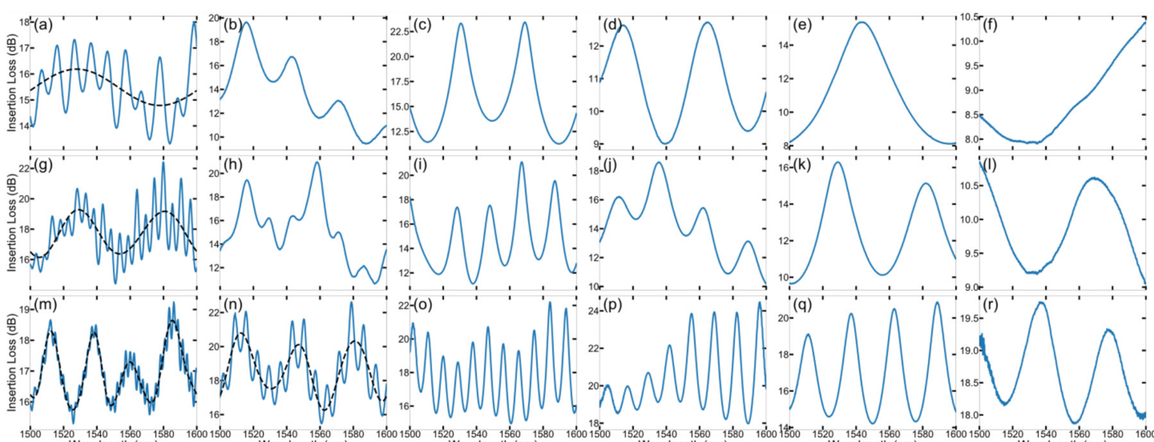

Fig. 5. Insertion losses of (top) 504 μm, (middle) 1012 μm, and (bottom) 2014 μm long suspended waveguides with a core diameter of 6.7 μm with the microfluidic channel empty (a,g,m), and while surrounded by a fluid with a refractive index at 1550 nm of (b,h,n) 1.2960, (c,i,o) 1.3350, (d,j,p) 1.3730, (e,k,q) 1.4140 and (f,l,r) 1.4380. To facilitate the analysis, each plot has a specific y-scale. The dashed line in (a,g,m,n) represents the secondary modulation.

sertion losses (IL) are described by:

$$\mathrm{IL}(\lambda) = -10\log_{10}\left(\frac{1}{2}\left[+\cos\left(\frac{2\pi}{\lambda}L\left(n_{wvg} - n_{ch}\right)\right)\right]\right) \tag{2}$$

where λ is the vacuum wavelength, L is the length of the suspended waveguide, and n_{wvg} and n_{ch} are the effective refractive index of the fundamental mode of the suspended waveguide and refractive index of the cladding medium, respectively, with both being a function of the wavelength. By knowing the effective refractive index $n_{wvg}(\lambda)$, Eq. (2) can be numerically solved, and the expected free spectral range retrieved. Given that the diameter of the suspended core and the refractive index difference is smaller than unity for all external fluids, the calculation of the effective refractive index is simplified by considering the weakly guiding approximation. Accordingly, $n_{wvg}(\lambda)$ is determined from the following characteristic equations:

$$V\sqrt{1-b}\,\frac{J_{l+1}\left(V\sqrt{1-b}\right)}{J_l\left(V\sqrt{1-b}\right)} = V\sqrt{b}\,\frac{K_{l+1}\left(V\sqrt{b}\right)}{K_l\left(V\sqrt{b}\right)} \tag{3}$$

$$V = \frac{\pi}{\lambda}\times d\times\sqrt{n_{core}^2 - n_{cladding}^2} \tag{4}$$

$$b = \frac{n_{wvg}^2 - n_{core}^2}{n_{core}^2 - n_{cladding}^2} \tag{5}$$

where J_l and K_l are the Bessel functions of the first kind and the modified Bessel functions of the second kind of order l, respectively, V is the generalized frequency, b is the generalized waveguide index, d is

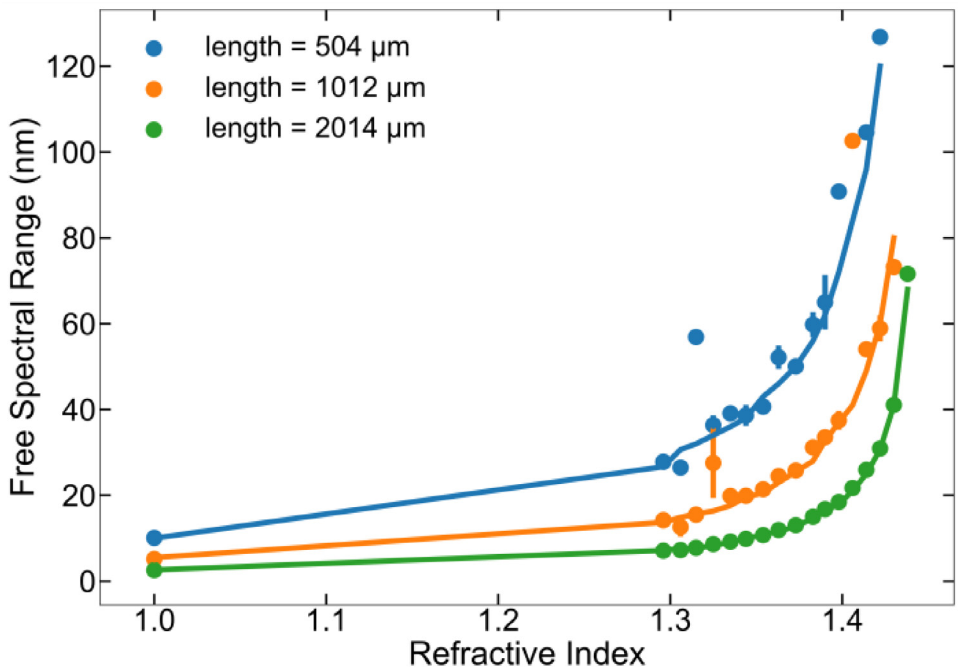

Fig. 6. Experimental (scatter points) and theoretical (solid line) period of the main modulation observed in the spectra of Fig. 5. The theoretical curve was numerically determined by considering the interference between the fundamental mode of a suspended waveguide with core diameter of 6.7 μm and uncoupled light that travels across the channel. The refractive index in the x-axis corresponds to the refractive index of the cladding at 1550 nm.

the diameter of the suspended core, and n_{core} and $n_{cladding}$ are the refractive indices of the core and cladding, respectively [25]. By knowing the diameter of the suspended core and the refractive index profiles of the core and cladding, the effective refractive index $n_{wvg}(\lambda)$ can be determined numerically for all tested conditions. The theoretical expected free spectral range for the three lengths of the suspended waveguide tested is also plotted in Fig. 6. The expected curves match well with the experimental data, with the Spearman's rank correlation being 0.914, 0.946 and 0.998 for the 504, 1012 and 2014 μm long suspended waveguides, respectively. We can then conclude that the main modulation in the insertion loss spectra of Figs. 3 and 5 is due to interference between the LP_{01} mode of the suspended waveguide and light that is uncoupled and travels unguided across the channel. This also indicates that the device could be used as a refractometer, with the suspended waveguide as reference arm and the microfluidic channel as sensing arm, either by monitoring variations in the position of the resonant peak or of the free spectral range.

Still, Figs. 5(a,g,m,n) show a lower-frequency modulation which is outlined in the respective figures by a dashed curve. This secondary oscillation is only observed in those conditions where the suspended waveguide supports multimode propagation. Following a similar analysis, we conclude that the measured period does not coincide with the expected free spectral range if interference between higher-order modes and unguided light is considered. Instead, the measured period points towards this lower-frequency modulation being a result of modal interference between the LP_{01} and the LP_{02} modes of the suspended waveguide. This was numerically confirmed by again solving Eqs. (3-5) in order to determine the effective refractive index of the modes LP_{01} and LP_{02}, and then by replacing the computed values in Eq. (2) to determine the theoretical free spectral range. Modal interference, as described here, has already been used to create modal interferometers in single-mode – multimode – single-mode fiber configurations [26]. Further, re-examining the geometry of the propose device, it mirrors that of an abrupt tapered fiber with the lead-in and suspended waveguide axially aligned. In these conditions, it is documented that most of the optical power is coupled to symmetric modes and that it is mostly carried by the LP_{01} and LP_{02} modes [27–28].

To remove both modulations from the transmission spectra, curved suspended waveguides should be designed to filter out higher-order modes [8] and to separate the guided light from the uncoupled incident light [15]. Still, and despite being possible to fabricate tapered waveguides [5], the design of curved waveguides through the proposed procedure is hindered by material reflow occurring during thermal treatment. Nonetheless, these configurations can be achieved if thermal annealing is dropped from the fabrication protocol, as chemical etching itself does not alter the geometry of the suspended waveguide. This, however, would be done at the expense of a rougher surface, which is linked to optical scattering and higher propagation losses.

4. Conclusion

In this work, suspended silica-core liquid-cladding waveguides were fabricated inside a microfluidic channel through fs-laser direct writing followed by chemical etching and thermal annealing. The inclusion of thermal treatment was necessary to reduce the surface roughness of the machined waveguide to 11 nm, and to morph the core's cross-section into a circular shape. Straight waveguides with a minimum core diameter of 3.8 μm were fabricated. The proposed methodology provides a wide control over the dimensions and shape of the suspended core. The geometry of the waveguide can be tailored by carefully patterning the irradiation pattern, as we have also shown in [5]. Further, fine tuning of the dimensions of the core can be obtained by adding a post-processing chemical etching procedure.

The insertion losses are mainly affected by the coupling losses between the lead-in/lead-out and the suspended waveguide. In particular, the mode profile of the suspended waveguide can be changed by adjusting the refractive index of the fluidic medium, which enables tuning of the coupling loss. Further, the transmission spectra contain two periodical behaviors: a high-frequency modulation linked to Mach-Zehnder interference between the fundamental mode of the suspended waveguide and light that is uncoupled and travels unguided across the microfluidic channel, and a low-frequency modulation observed when the suspended waveguide supports multimode propagation and attributed to modal interference between the LP_{01} and LP_{02} modes. By tracking the position of the resonant peaks or by monitoring the variation in the free spectral range, the presented device can be used as an interferometric optical sensor.

5. Author Contributions

João M. Maia and P. V. S. Marques conceived the device. João M. Maia fabricated the device, with assistance by Vítor A. Amorim who determined the writing parameters that minimize the insertion losses of the lead-in and lead-out waveguide. João M. Maia performed the measurements. All authors contributed to the analysis and discussion of the results. João M. Maia and P. V. S Marques wrote the manuscript, which was reviewed by all authors.

Declaration of Competing Interest

The authors declare that they have no known competing financial interests or personal relationships that could have appeared to influence the work reported in this paper.

Acknowledgments

This work was supported by Fundação para a Ciência e a Tecnologia through grant no. SFRH/BD/133095/2017.

References

[1] Choudhury D, Macdonald JR, Kar AK. Ultrafast laser inscription: perspectives on future integrated applications. Laser Photonics Rev 2014;8(6):827–46.
[2] Crespi A, Gu Y, Ngamsom B, Hoekstra HJWM, Dongre C, Pollnau M, et al. Three-dimensional Mach-Zehnder interferometer in a microfluidic chip for spatially-resolved label-free detection. Lab Chip 2010;10(9):1167–73.
[3] Maia JM, Amorim VA, Viveiros D, Marques PVS. Magnetic field sensors in fused silica fabricated by femtosecond laser micromachining. J Phys 2020;2(1):015003.
[4] Bellini N, Vishnubhatla KC, Bragheri F, Ferrara L, Minzioni P, Ramponi R, et al. Femtosecond laser fabricated monolithic chip for optical trapping and stretching of single cells. Opt Express 2010;18(5):4679–88.
[5] Maia JM, Amorim VA, Viveiros D, Marques PVS. Femtosecond laser micromachining of an optofluidics-based monolithic whispering-gallery mode resonator coupled to a suspended waveguide. Sci Rep 2021;11:9128.
[6] Prabhakar A, Verma D, Dhwaj A, Mukherji S. Microchannel integrated tapered and tapered-bend waveguides, for proeficient, evanescent-field absorbance based, on-chip, chemical and biological sensing operations. Sens Actuators, B 2021;332(1):129455.
[7] Liu Z, Xu J, Lin Z, Qi J, Li X, Zhang A, et al. Fabrication of single-mode circular optofluidic waveguides in fused silica using femtosecond laser microfabrication. Opt Laser Technol 2021;141:107118.
[8] Sun H, He F, Zhou Z, Cheng Y, Xu Z, Sugioka K, et al. Fabrication of microfluidic optical waveguides on glass chips with femtosecond laser pulses. Opt Lett 2007;32(11):1536–8.
[9] Jiang L, Pau S. Integrated waveguide with a microfluidic channel in spiral geometry for spectroscopic applications. Appl Phys Lett 2007;90(11):11108.
[10] Barshilia D, Chau L-K, Chang G-E. Low-cost planar waveguide-based optofluidic sensor for real-time refractive index sensing. Opt Express 2020;28(19):27337–45.
[11] Zhang Y, Kenarangi F, Zhang H, Vaziri S, Li D, Pu X, et al. Versatile optofluidic solid–core/liquid-cladding waveguide based on evanescent wave excitation. Anal Chem 2020;92(22):14983–9.
[12] Casamenti E, Yang T, Vluger P, Bellouard Y. Vibration monitoring based on optical sensing of mechanical nonlinearities in glass suspended waveguides. Opt Express 2021;29(7):10853–62.
[13] Spagnolo M, Motta R, Memeo R, Pellegatta F, Crespi A, Osellame R. Resonant opto-mechanical modulators and switches by femtosecond laser micromachining. Opt Express 2020;28(16):23133–42.
[14] Ceccarelli F, Atzeni S, Pellegatta F, Pentangelo C, Crespi A, Osellame R. Low-power reconfigurable photonic integrated circuits fabricated by femtosecond laser micromachining. In: Proceedings of SPIE 11283; 2020.
[15] Kelemen L, Lepera E, Hórvath B, Ormos P, Osellame R, Vázquez RM. Direct writing of optical microresonators in a lab-on-a-chip for label-free biosensing. Lab Chip 2019;19(11):1985–90.
[16] Cheng Y, Sugioka K, Midorikawa K. Freestanding optical fibers fabricated in a glass chip using femtosecond laser micromachining for lab-on-a-chip application. Opt Express 2005;13(18):7225–32.
[17] Osawa K, Inoue H, Masuno A, Katayama K, Zhang Y, Utsuno F, et al. Smoothing of surface of silica glass by heat treatment in wet atmosphere. J Appl Phys 2011;10(9):103520.
[18] Drs J, Kishi T, Bellouard Y. Laser-assisted morphing of complex three dimensional objects. Opt Express 2005;13(18):7225–32.
[19] Amorim VA, Maia J, Viveiros D, Marques PVS. Loss mechanisms of optical waveguides inscribed in fused silica by femtosecond laser direct writing. J Lightwave Technol 2019;37(10):2240–5.
[20] Kazansky PG, Yang W, Bricchi E, Bovatsek J, Arai A, Shimotsuma Y, et al. Quill writing with ultrashort light pulses in transparent materials. Appl Phys Lett 2007;90(15):151120.
[21] Witcher JJ, Reichman WJ, Fletcher LB, Troy NW, Krol DM. Thermal annealing of femtosecond laser written structures in silica glass. Opt Mater Express 2013;3(4):502–10.
[22] Saruwatari M, Nawata K. Semiconductor laser to single-mode fiber coupler. Appl Opt 1979;18(11):1847–56.
[23] Yu X, Li G, Liu S, Zhang J, Chen X, Zhang L, et al. Characteristics of in-fiber Mach-Zehnder interferometer formed by lateral offset splicing. Proc SPIE 2012;8561.
[24] Duan D-W, Rao Y-J, Xu L-C, Zhu T, Wu D, Yao J. In-fiber Mach-Zehnder interferometer formed by large lateral offset fusion splicing for gases refractive index measurement with high sensitivity. Sens Actuators, B 2011;160(1):1198–202.
[25] Chen C-L. Foundations for guided-wave optics. In: chapter 9. John Wiley & Sons; 2006. p. 225–57. pages.
[26] Wang Q, Farrell G. All-fiber multimode-interference-based refractometer sensor: proposal and design. Opt Lett 2006;31(3):317–19.
[27] Tian Z, Yam SS. In-line single-mode optical fiber interferometric refractive index sensors. J Lightwave Technol 2009;27(13):2296–306.
[28] Xu W, Shen Y, Yu C, Dong B, Zhao W, Wang Y. Long modal interference in multimode fiber and its application in vital signs monitoring. Opt Commun 2020;474:126100.